RSC Advances

PAPER

View Article Online
View Journal | View Issue

Cite this: *RSC Adv.*, 2025, **15**, 30404

Sensitive detection of amantadine in food matrices using DTT-functionalized gold nanoparticles

Glowi Alasiri,[a] Ali M. Alaseem,[b] Al-Montaser Bellah H. Ali,[c] Ramadan Ali[d] and Mohamed M. El-Wekil *[c]

Detecting amantadine (AMD) residues in food is essential due to its illegal use in livestock for disease prevention and growth promotion, practices that can lead to harmful drug residues in meat, eggs, and milk. Such residues pose significant public health concerns, including the development of drug-resistant pathogens. In this study, a highly sensitive and selective fluorometric method is presented for detecting AMD in food matrices. The assay is based on the formation of a fluorescent isoindole derivative *via* a ternary reaction between *o*-phthalaldehyde (OPA), the primary amine group of AMD, and dithiothreitol (DTT) on citrate-stabilized gold nanoparticles (C-AuNPs) functionalized with DTT (DTT@C-AuNPs) under alkaline conditions. DTT acts as a bifunctional linker, anchoring to the nanoparticle surface through one SH group, while the second SH remains available to participate in isoindole formation. This configuration results in a turn-on fluorescence system, with emission observed at λ_{ex} = 330 nm and λ_{em} = 460 nm, overcoming the typical quenching associated with AuNPs-based sensors. The method demonstrated LOD of 20 nM and high anti-interference/selectivity toward AMD, with minimal interference from matrix components. Validation through standard addition recovery experiments in AMD-spiked food samples confirmed the assay's accuracy and precision. Overall, this fluorometric platform offers a rapid, reliable, and cost-effective approach for AMD monitoring, supporting its practical application in food quality control and regulatory surveillance programs.

Received 18th July 2025
Accepted 14th August 2025

DOI: 10.1039/d5ra05197e

rsc.li/rsc-advances

1. Introduction

Amantadine (AMD) is a tricyclic amine compound used primarily to treat influenza A and Parkinson's disease. Its antiviral mechanism involves inhibiting the M2 proton channel of the influenza A virus, thereby preventing viral uncoating and replication.[1,2] Additionally, AMD exerts neurological effects by modulating glutamatergic neurotransmission through the blockade of *N*-methyl-D-aspartate (NMDA) receptors. However, the unauthorized use of AMD in poultry farming raises significant public health concerns. Residues in poultry products can compromise food safety and contribute to reduced therapeutic efficacy in humans, potentially leading to neurological side effects such as dizziness, hallucinations, and confusion.[3] Moreover, the widespread and unregulated use of AMD has accelerated the development of drug-resistant and highly mutative viral strains, undermining its effectiveness as an antiviral agent.[4] Due to these risks, regulatory authorities in several countries have banned the use of AMD in poultry production to safeguard both human health and the integrity of the food supply chain.[5,6] Consequently, the development and implementation of sensitive, reliable, and user-friendly analytical methods for detecting AMD residues in food products are critical for ensuring regulatory compliance and protecting public health.

The need to monitor AMD for food safety has driven the development of diverse detection techniques. For examples, plasmonic immunoassay,[7] colorimetry,[8] immunochromatography,[9,10] and electrochemistry[11,12] were developed for determination of AMD. Despite the availability of various analytical techniques for AMD detection, many suffer from notable drawbacks: immunoassays require costly antibodies and may exhibit cross-reactivity; electrochemical platforms often require complex electrode modification and are susceptible to matrix fouling; and conventional OPA/thiol fluorometric assays lack the sensitivity to reliably detect trace AMD in complex food samples. These limitations underscore the need for a simple, rapid, and cost-effective method capable of achieving sub-μM detection limits in real matrices while maintaining high selectivity. To address this gap, we developed a DTT-functionalized gold nanoparticle (DTT@C-AuNP) platform that enables the

[a]*Department of Biochemistry, College of Medicine, Imam Mohammad Ibn Saud Islamic University (IMSIU), Riyadh, 13317, Saudi Arabia*

[b]*Department of Pharmacology, College of Medicine, Imam Mohammad Ibn Saud Islamic University (IMSIU), Riyadh, Saudi Arabia*

[c]*Department of Pharmaceutical Analytical Chemistry, Faculty of Pharmacy, Assiut University, Assiut, Egypt. E-mail: mohamed.elwakeel@pharm.aun.edu.eg; mohamed.mohamoud@ymail.com*

[d]*Department of Pharmaceutical Chemistry, Faculty of Pharmacy, University of Tabuk, Tabuk 71491, Saudi Arabia*

surface-confined formation of fluorescent isoindole derivatives upon reaction with AMD. This "turn-on" system overcomes the typical quenching observed in AuNP-based sensors by leveraging nanoscale surface effects to enhance fluorescence quantum yield, enabling sensitive, selective, and rapid AMD detection in diverse food matrices in compliance with regulatory zero-tolerance requirements. Fluorometric-based sensors stand out for their simplicity, rapid response, high sensitivity, and excellent selectivity in detecting a wide range of analytes.[13–15]

2-Mercaptoethanol and *o*-phthalaldehyde (OPA) are commonly employed reagents for the fluorogenic detection of primary amines. Under alkaline conditions at room temperature, they react with primary amines to form highly fluorescent isoindole derivatives, enabling sensitive and selective analysis.[16,17] For instance, Qi *et al.* employed a reaction system using OPA and thiol-containing acid at alkaline medium for the colorimetric determination of putrescine, achieving a detection limit of 0.44 μM.[18] Similar strategies have been reported using other functionalized nanostructures; for instance, fluorescein isothiocyanate (FITC)-functionalized magnetic core–shell nanoparticles have been applied for selective target detection, demonstrating the versatility of surface functionalization in enhancing analytical performance.[19] These precedents support the design rationale of our DTT-functionalized AuNP system for turn-on fluorescence detection of AMD in complex matrices.

Gold nanoparticles (AuNPs) are extensively utilized in colorimetric and fluorometric sensing applications owing to their exceptionally high extinction coefficients, which surpass those of conventional organic dyes. When fluorophores or labeled receptors interact with AuNPs, fluorescence quenching often occurs *via* energy or electron transfer mechanisms.[20] In contrast, "turn-on" fluorescence approaches rely on the restoration or enhancement of fluorescence intensity in the presence of the target analyte, enabling sensitive and selective detection as the analyte concentration increases.[21]

Here, a "turn-on" fluorometric platform based on dithiothreitol-functionalized gold nanoparticles (DTT@AuNPs) and OPA was prepared for sensing of AMD. One thiol anchored DTT to AuNPs while the free thiol participates in OPA–AMD condensation, forming a rigid isoindole directly at the nanoparticle interface. This confined microenvironment accelerates fluorophore formation, suppresses non-productive quenching typical of Au-based systems, and yields a robust signal increase at λ_{ex} = 330 nm/λ_{em} = 460 nm. The resulting assay is rapid, simple, and low-cost, while achieving a low limit of detection (~0.02 μM; ≈3.2 μg L^{-1}) and a wide linear range—performance suitable for trace-level AMD monitoring in real food matrices and aligned with regulatory surveillance needs.

2. Experimental

2.1. Chemicals and instrumentation

Amantadine (AMD, 98.6%), *o*-phthalaldehyde (OPA, 98.4%), mercaptoethanol (97.8%), tetrachloroauric acid ($HAuCl_4 \cdot 3H_2O$, 99.9%), sodium dodecyl sulphate (SDS, AR), 1,4-dithioerythritol (DTT, 97.5%), trisodium citrate (97.7%), acyclovir (98.3%), ribavirin (96.9%), olaquindox (98.5%), enrofloxacin (97.8%), moxifloxacin (97.2%), ciprofloxacin (98.6%), ofloxacin (99.2%), sulfamethazine (97.7%), tetracycline (98.3%), oxytetracycline (98.4%), florfenicol (97.6%), chloramphenicol (98.9%), metronidazole (97.4%), trichloroacetic acid (AR), HCl, and NaOH were procured from Sigma Aldrich, Germany.

Fluorescence and UV-vis spectra were recorded on Shimadzu RF-5301 PC and 1601 PC instruments (Tokyo, Japan). Zeta potential was determined using a ZEN 3600 Nano ZS instrument (Malvern, UK). Transmission electron microscopy (TEM, JEOL JEM-100CX II, USA) was employed to characterize AuNPs. Fourier transform infrared (FT-IR) spectra were acquired using the Nicolet™ iSTM10 spectrograph (Varian Instrument Co., Ltd, USA).

2.2. Synthesis of citrate-stabilized gold nanoparticles (C-AuNPs)

The synthesis of citrate-stabilized gold nanoparticles (C-AuNPs) was carried out following the method described in ref. 22, with minor modifications. A 1.18 mM solution of $HAuCl_4 \cdot 3H_2O$ was brought to a boil under reflux, after which 10 mL of 40.67 mM trisodium citrate was added. The reaction mixture was maintained under reflux for 18 minutes, resulting in the formation of a red-colored solution. The mixture was then stirred at room temperature until fully cooled.

2.3. Synthesis of DTT@C-AuNPs

DTT (30 mg mL^{-1}, dissolved in borate buffer at pH 10.0) was mixed with C-AuNPs at various volume ratios (10 : 1, 8 : 3, 7 : 4, 5 : 2, 3 : 7, 4 : 9, and 3 : 3, v/v) and shaken for 12 hours. Subsequently, 3 mL of the resulting dispersion was centrifuged at 10 000 rpm for 30 minutes, washed three times with double-distilled water (DDW), and re-dispersed in 3 mL of DDW. Residual free DTT was removed through repeated centrifugation and washing steps.

2.4. Detection of AMD using DTT@C-AuNPs/OPA system

In a 5.0 mL volumetric flask, 100 μL of DTT@C-AuNPs was combined with 400 μL of 3.5% SDS and 500 μL of borate buffer (pH 9.7). Subsequently, 500 μL of 10.0 mM OPA was added, and the mixture was incubated at room temperature for 3 minutes. Next, 300 μL of the AMD standard solution was introduced, and the volume was adjusted to the mark with DDW. The resulting solution was further incubated at room temperature for 5 minutes. Fluorescence intensity was then measured under the specified wavelength settings, and the change in fluorescence intensity (ΔF) was plotted against AMD concentration to generate the calibration curve.

2.5. Detection of AMD using traditional OPA reagent

Into a 5.0 mL volumetric flask, 500 μL of AMD solution at varying concentrations was added, followed by 500 μL of borate buffer (pH 9.7). Subsequently, 300 μL of 1.5% (v/v) 2-mercaptoethanol and 500 μL of 5.0 mM OPA were introduced. The mixture was then diluted to volume with DDW and incubated at

room temperature for 10 minutes to allow complete reaction. Fluorescence measurements were recorded at an emission wavelength of 455 nm, following excitation at 330 nm.

2.6. Real sample analysis

Real samples—including egg, duck muscle and chicken breast—were obtained from local markets. The samples were homogenized and subsequently spiked with varying concentrations of AMD. Following this, 1.5 mL of trichloroacetic acid was added to each sample, and the mixture was vortexed for 15 minutes. The resulting mixture was centrifuged at 6000 rpm for 20 minutes, followed by filtration. The obtained filtrate was then subjected to analysis using the proposed fluorometric method.

3. Results and discussions

3.1. Choice of DTT@c-AuNPs and characterization

Due to their unique optical properties and strong affinity for SH groups; AuNPs are widely utilized as effective sensing materials.[23] The formation of Au–S bonds is highly pH-dependent: under acidic conditions, SH groups remain protonated, hindering their ability to bind to Au surfaces. Conversely, alkaline conditions promote SH deprotonation, thereby enhancing Au–S bond formation.[24] Notably, the strength of Au–S bonds is comparable to that of Au–Au bonds, meaning that SH adsorption can significantly alter the interparticle interactions and assembly behavior of AuNPs.[25] This sensitivity to the chemical environment makes AuNPs particularly valuable in the design of responsive and tunable nanosensors. 1,4-Dithioerythritol (DTT) is a widely used thiol-protecting and reducing agent in protein and peptide chemistry, employed to maintain SH groups in their reduced form and to cleave disulfide bonds, thereby preventing oxidative cross-linking.[26] In the context of ligand exchange on gold nanoparticles (AuNPs), DTT and other thiol-containing molecules can effectively displace surface-adsorbed citrate ions. This exchange is thermodynamically favored due to the substantial difference in bond strength between Au–S (~40 kcal mol^{-1}) and Au–O–COOH (~2 kcal mol^{-1}) interactions. The efficiency and kinetics of this replacement process are further modulated by multiple factors, including chelation effects, electronic interactions, steric hindrance, solvent polarity, and the dynamic nature of the ligand shell.[27] These factors collectively influence the surface functionalization, colloidal stability, and subsequent applications of AuNPs in sensing, catalysis, and bioconjugation.

Herein, Au^{3+} ions were reduced to AuNPs with an average diameter of 11.87 nm using citrate as both reducing and stabilizing agent. C-AuNPs were functionalized with DTT (pK_a 8.43) in pH 9.7 borate buffer, leveraging the strong nucleophilicity and metal-binding affinity of SH. TEM images and localized surface plasmon resonance spectra of both C-AuNPs and DTT@C-AuNPs were recorded against DDW (Fig. 1). The DTT@C-AuNPs colloid was obtained after overnight stirring and centrifugation at 10 000 rpm for 30 min. Prior to centrifugation, the localized surface plasmon resonance maximum appeared at 530 nm; post-centrifugation, this peak remained but exhibited a shoulder near 665 nm and a purple hue, suggesting nanoparticle convergence due to increased electrostatic interactions and altered surface potentials. Zeta potential measurements showed a shift from −6.47 mV (C-AuNPs) to −20.89 mV (DTT@C-AuNPs), increasing to −29.65 mV after centrifugation, indicating enhanced electrostatic repulsion and colloidal stability (Fig. 2). These findings confirmed the successful formation of DTT@C-AuNPs. Transmission electron microscopy (TEM) was employed to characterize the morphology and size distribution of citrate-stabilized gold nanoparticles (C-AuNPs) and DTT-functionalized nanoparticles (DTT@C-AuNPs) (Fig. 3). TEM analysis revealed that the average particle size increased from 11.87 ± 1.45 nm for C-AuNPs to approximately 13.2 ± 1.8 nm following DTT functionalization, consistent with the formation of an organic DTT layer on the

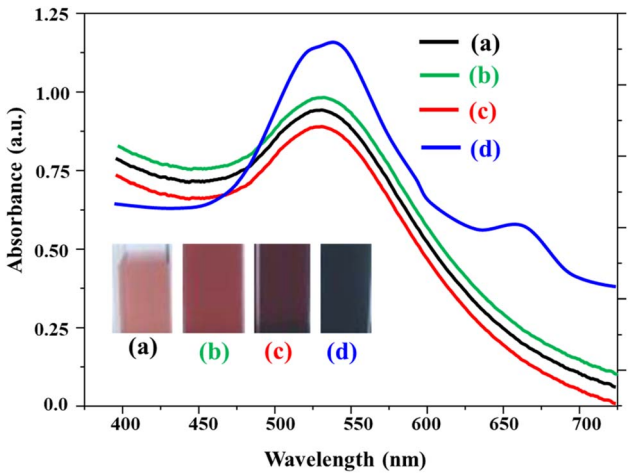

Fig. 1 Localized surface plasmon resonance spectra of (a) C-AuNPs in DDW, (b) C-AuNPs in borate buffer (pH 10.0), (c) DTT@C-AuNPs before centrifugation, and (d) centrifuged DTT@C-AuNPs.

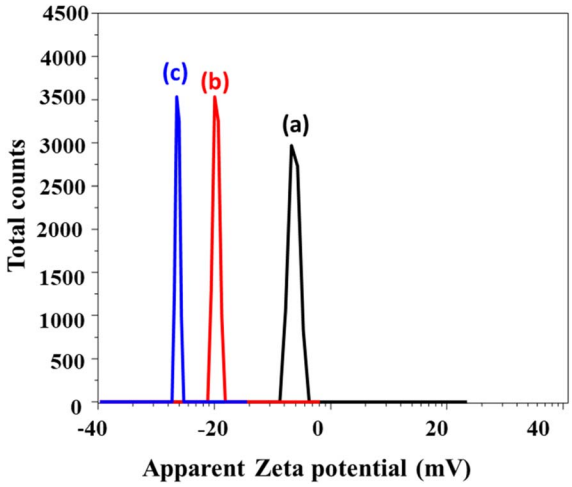

Fig. 2 Zeta potentials of (a) C-AuNPs in borate buffer (pH 10.0), (b) DTT@C-AuNPs before centrifugation, and (c) centrifuged DTT@C-AuNPs.

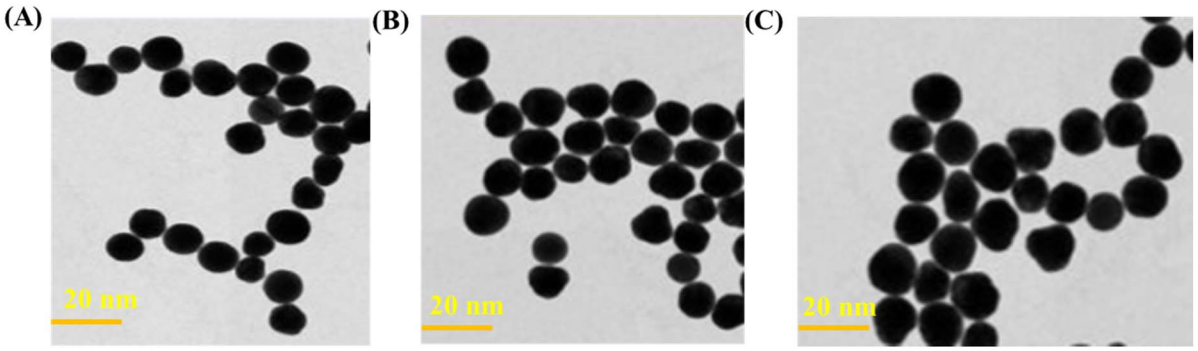

Fig. 3 TEM images of C-AuNPs (A), DTT@C-AuNPs (B), and DTT@C-AuNPs/50 μM AMD (C).

nanoparticle surface. Upon AMD interaction and isoindole formation, a further slight increase to ~13.9 ± 1.5 nm was observed, which may result from partial interparticle association or surface rearrangement during the condensation reaction. Importantly, these changes remained within the nanoscale range, and no extensive aggregation was detected, as confirmed by the retained colloidal stability and the linearity of the fluorescence response. The observed size evolution correlates well with the increase in negative zeta potential, confirming successful surface modification and enhanced electrostatic stabilization. TEM analysis, in conjunction with a red-shifted shoulder in the localized surface plasmon resonance (LSPR) spectra, the characteristic purple coloration of DTT@C-AuNPs, and the increase in negative surface charge, collectively confirmed successful surface functionalization with anionic thiolate ($-S^-$) groups derived from DTT. These findings indicate partial nanoparticle agglomeration—likely due to interparticle bridging *via* DTT—without progressing to irreversible aggregation. Importantly, this structural rearrangement did not adversely affect the sensitivity or performance of the nanoparticles in subsequent assays for AMD detection. The extent of agglomeration in AuNPs functionalized with short-chain dithiols is primarily governed by surface charge. Strong electrostatic repulsion between negatively charged particles can hinder the close proximity necessary for effective dithiol-mediated interparticle bridging. As a result, higher surface charge densities promote colloidal stability by limiting agglomeration, whereas reduced surface charge may facilitate partial or reversible clustering through dithiol linkages.[28] Co-adsorption of SH-containing ligands onto C-AuNPs can lead to the formation of a stabilized interparticle network, facilitated by hydrogen bonding among surface functional groups. These weak, non-covalent interactions between thiolated nanoparticles contributed to a loosely associated structure without inducing irreversible aggregation.[29] Importantly, such intermolecular interactions remained within a tolerable range, as they did not adversely affect the sensitivity or performance of the fluorometric assay for AMD detection. Another important situation is the quenching of OPA fluorescence by C-AuNPs *via* inner-filter effect (IFE). This strategy was proposed by Cayuela *et al.*[30] Briefly, the fluorescence of amine-functionalized carbon dots (CDs), which carry a positive surface charge, was quenched by citrate-functionalized silver nanoparticles (C-AgNPs) *via* the IFE. Subsequent aggregation of C-AgNPs—induced by electrostatic interactions with surface $-NH_2$ groups on the CDs—resulted in a red-shift of their plasmon band and restoration of CD fluorescence. This "switch-on" response enabled the quantitative detection of C-AgNPs, facilitated by amine-to-ammonium conversion under appropriate pH conditions. Notably, the induced nanoparticle agglomeration did not compromise the analytical accuracy of the fluorometric assay.

Fig. 4 presents the FT-IR spectra of C-AuNPs before and after functionalization with DTT, forming DTT@C-AuNPs. The characteristic absorption bands observed at 3312 cm^{-1}, 2824–2912 cm^{-1}, 2238 cm^{-1}, and 1670 cm^{-1} correspond to the stretching vibrations of hydroxyl (ν(OH)), aliphatic C–H (ν(CH)), thiol (ν(SH)), and the bending vibration of hydroxyl groups (δ(OH)), respectively. These functional groups are consistent with the chemical structure of DTT. Notably, after conjugation with C-AuNPs, these bands exhibited a shift toward lower wavenumbers, indicating successful surface functionalization. This shift suggests the formation of chemical interactions, likely through S–Au bonding, confirming the immobilization of DTT onto the nanoparticle surface. Moreover, the absorption band at 2238 cm^{-1} was disappeared as a result of Au–S covalent bond formation. Fig. 5 displays the EDX spectrum of DTT@C-AuNPs, revealing prominent elemental signals for carbon (C),

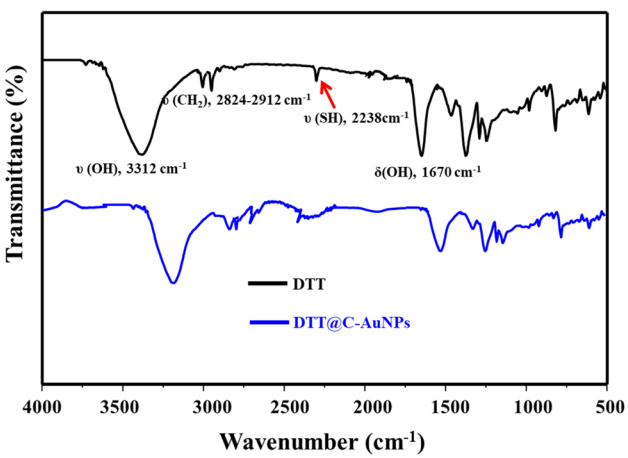

Fig. 4 FT-IR spectra of DTT and DTT@C-AuNPs.

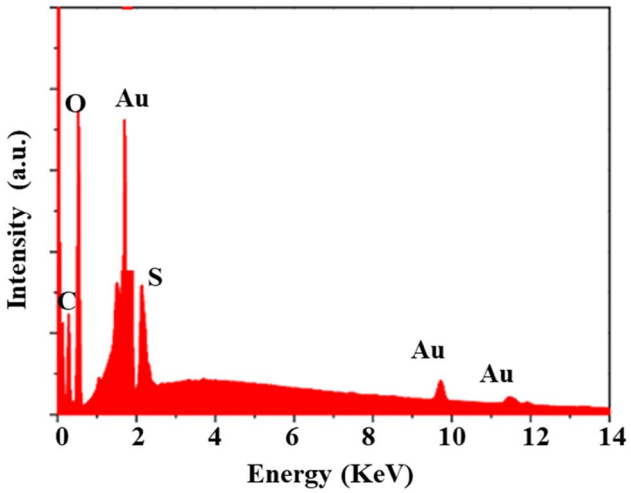

Fig. 5 EDX spectrum of DTT@C-AuNPs.

oxygen (O), sulfur (S), and gold (Au). The presence of sulfur, in particular, supports the covalent attachment of SH-containing DTT to the gold surface, while the signals of C and O further confirm the organic nature of the functionalized layer.

3.2. Possible detection mechanism

In the proposed sensing system, citrate-stabilized gold nanoparticles (C-AuNPs) serve multiple mechanistic roles beyond acting as inert scaffolds. First, their strong affinity for thiol groups allows stable immobilization of DTT *via* Au–S covalent bonding, which leaves the second thiol group of DTT available for condensation with OPA and the primary amine group of AMD to form the fluorescent isoindole. This surface-anchored configuration positions reactive groups in close proximity, enhancing the reaction rate and fluorescence quantum yield. Second, the AuNP surface acts as a nano-catalytic platform that can accelerate isoindole formation *via* localized microenvironment effects, such as concentrating reactants and promoting thiol–amine–aldehyde condensation under mild conditions. Third, AuNPs influence the photophysical behavior of the system: in the absence of AMD, the proximity of OPA to the AuNP surface results in fluorescence quenching *via* energy or electron transfer. Upon isoindole formation, the rigid, surface-bound fluorophore experiences reduced non-radiative decay and diminished AuNP-induced quenching, giving rise to a "turn-on" fluorescence signal. Finally, the colloidal stability imparted by the DTT functional layer ensures reproducible signal generation without irreversible aggregation, maintaining assay sensitivity over the tested concentration range.

Inner-filter effect (IFE) occurs when an absorber's spectrum overlaps with a fluorophore's, reducing fluorescence *via* reabsorption (secondary IFE).[31] This causes a non-linear signal at higher concentrations. Unlike traditional IFE-based methods,[32] the as-prepared surface reaction produced a new fluorescent species, avoiding IFE effects. As a result, our fluorescence-concentration data remained linear (Section 3.4). In this case, no significant spectral overlap or absorption at the excitation/emission wavelengths is present from background components (AuNPs, DTT, or buffer) at the working dilution. After the dilution step (~50×), the absorbance of DTT@C-AuNPs at 440–460 nm is only ~0.04, well below the level where IFE becomes significant. Typically, IFE distortion is a concern at absorbance > 0.1.[33] In the present study, a novel "turn-on" fluorescence sensor was developed for the selective detection of aliphatic amine-containing compounds such as AMD. The sensing mechanism is based on the formation of a highly fluorescent isoindole derivative through a condensation reaction involving OPA, DTT, and the target amine (AMD), as illustrated in Scheme 1. Unlike conventional fluorescence modulation systems, this approach relies on *in situ* generation of the fluorescent species as the reaction product, rather than alteration of an existing fluorophore. The reaction proceeds rapidly under mild conditions, offering a sensitive and specific platform for AMD detection.

3.3. Optimization of variables

To optimize the experimental conditions for the assay, several parameters were systematically investigated, including the volume ratio of DTT to C-AuNPs at varying proportions (10 : 1, 8 : 3, 7 : 4, 5 : 2, 3 : 7, 4 : 9, and 3 : 3, v/v), the total volume of DTT-functionalized C-AuNPs (DTT@C-AuNPs) ranging from 20 to 160 μL, SDS concentration (0–5.0%, w/v), pH values (8.0–10.2), and reaction time intervals (1.0–10.0 minutes). As illustrated in Fig. 6, the optimal conditions were determined to be: a DTT : C-AuNPs volume ratio of 3 : 3 (v/v), 100 μL of DTT@C-AuNPs, SDS concentration of 3.5% (w/v), pH 9.7, a reaction time of 5 minutes, and OPA concentration of 10.0 mM. It was observed that increasing the SDS (improves dispersion of DTT@C-AuNPs) concentration beyond 3.5% (w/v) led to a decrease in fluorescence emission. This reduction is likely due to the excess SDS disrupting the surface functionalization of DTT@C-AuNPs, potentially through competitive adsorption or micelle formation, which interferes with the catalytic activity or the surface-enhanced formation of the fluorescent isoindole product. Consequently, the overall fluorescence efficiency is diminished. Additionally, at pH values exceeding 9.7, a decline in fluorescence intensity was also noted. This effect is presumably attributed to the reduced stability of the isoindole product under highly alkaline conditions, which may lead to its degradation or structural alteration, thereby compromising its fluorescent properties.[34] An excessive concentration of OPA above 10.0 mM resulted in a noticeable decrease in fluorescence emission. At elevated concentrations, OPA molecules may undergo self-quenching due to intermolecular interactions or aggregate formation. Additionally, excess OPA can react non-specifically or interact with accumulated reaction byproducts, facilitating non-radiative energy transfer pathways. These phenomena reduce the quantum yield and overall fluorescence intensity, thereby compromising the assay's sensitivity and performance.[35]

3.4. Detection of AMD

The proposed DTT@C-AuNPs/OPA-based fluorometric method (Scheme 1) and the conventional OPA method (Scheme 2) were

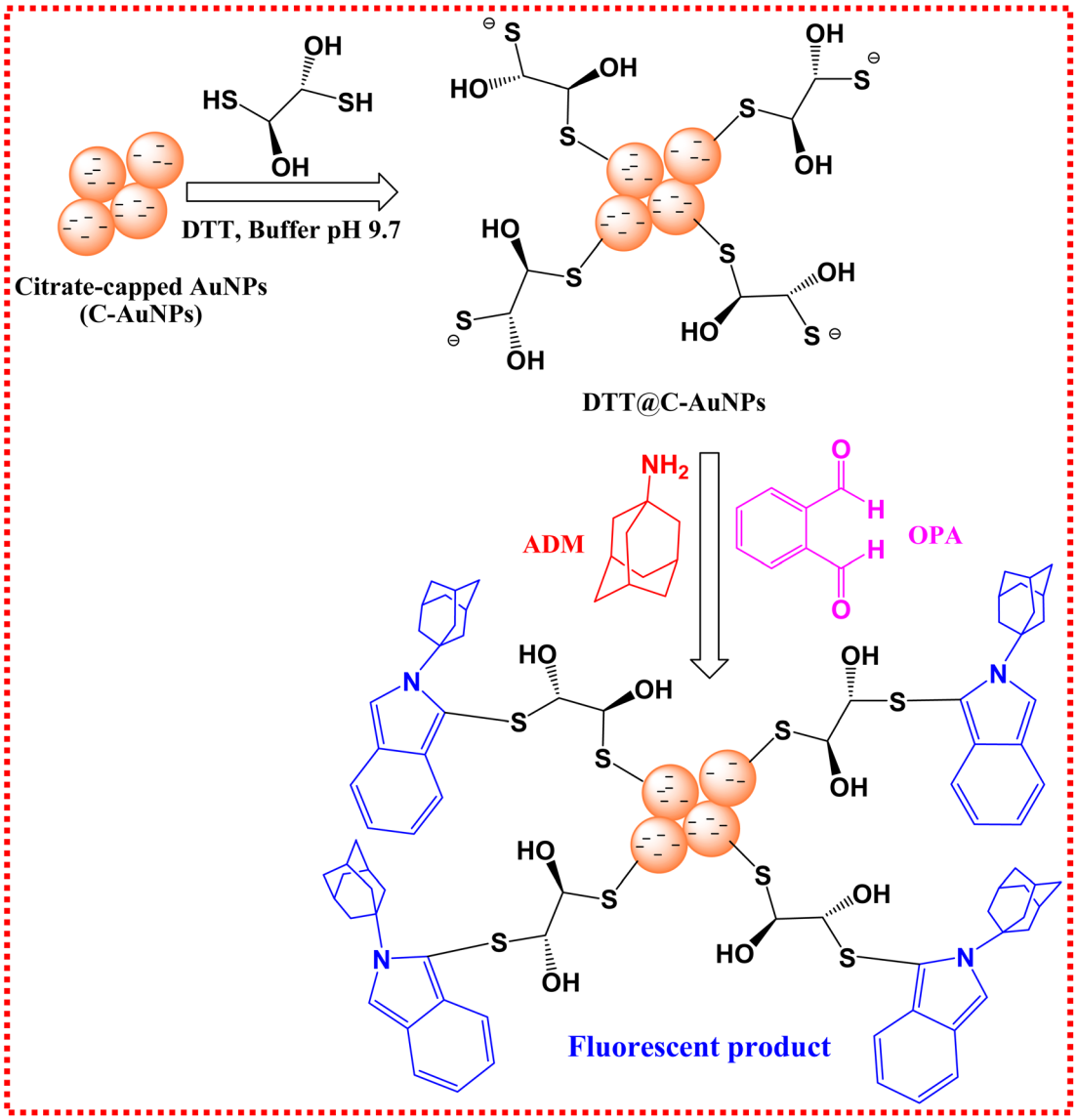

Scheme 1 Graphical representation for detection of AMD using DTT@C-AuNPs/OPA system.

employed for the quantitative detection of AMD. As illustrated in Fig. 7A, the DTT@C-AuNPs/OPA system exhibited a concentration-dependent increase in fluorescence intensity over the range of 0.1–250 μM AMD. A strong linear correlation was observed between the fluorescence change (ΔF) and AMD concentration, described by the regression equation $\Delta F = 27.479 + 1.177$ [AMD] with a correlation coefficient (R^2) of 0.9987 (Fig. 7B). The limit of detection (LOD), calculated based on a signal-to-noise ratio (S/N) of 3, was determined to be 0.02 μM. In contrast, the traditional OPA method demonstrated a narrower linear detection range of 1–220 μM, as shown in Fig. 8A. The corresponding linear regression equation was $\Delta F = 19.527 + 0.5399$ [AMD], with an R^2 of 0.9970 (Fig. 8B), and the calculated LOD was 0.28 μM. These results clearly indicate that the DTT@C-AuNPs/OPA system offers significantly enhanced sensitivity, with an LOD approximately 140-fold lower than that achieved by the conventional OPA method. This substantial improvement underscores the superior performance of the proposed nanomaterial-assisted protocol for trace-level detection of AMD. The LOD of the proposed method is comparable or even lower than some reported methods for determination of AMD (Table 1).

The achieved LOD of 0.02 μM (≈3.2 μg L^{-1}) in aqueous solution corresponds to a concentration well below the regulatory threshold for AMD residues in food matrices, which are effectively zero-tolerance according to both FDA and EU standards.[41,42] Given that typical extraction and dilution factors used in our protocol yield final test-solution concentrations in the low μg L^{-1} range for contaminated samples; this sensitivity ensures that our method can reliably identify prohibited AMD residues in compliance testing.

3.5. Interday and intraday precision

The synthesized DTT@C-AuNPs probe was employed to quantify AMD at three concentration levels (1.0, 50.0, and 200.0 μM)

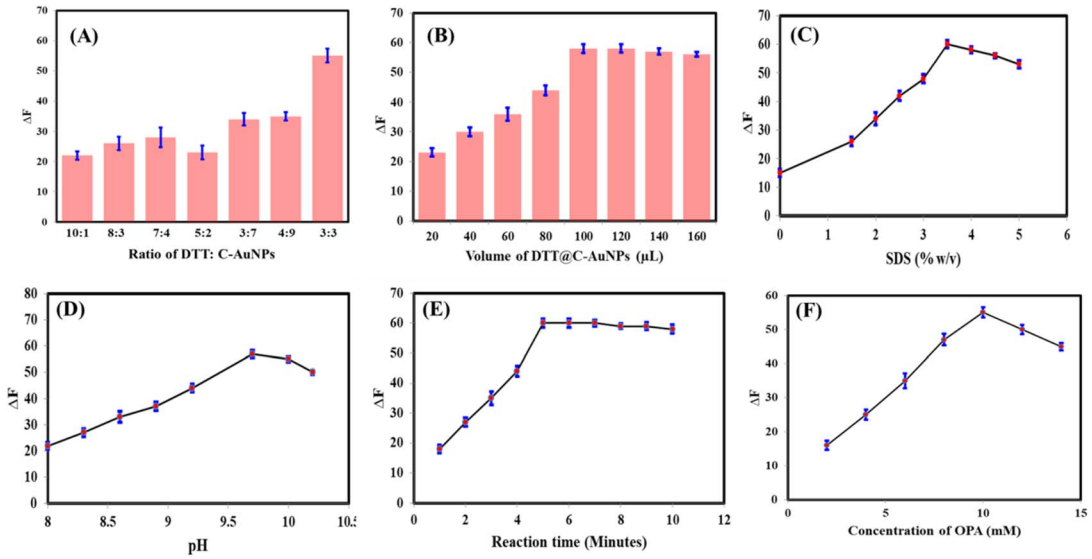

Fig. 6 Optimization of the detection conditions using 20.0 μM AMD: (A) ratio of DTT : C-AuNPs, (B) volume of DTT@C-AuNPs, (C) SDS concentration, (D) pH value, (E) reaction time, and (F) concentration of OPA. Data are shown as mean ± standard deviation (SD) from three independent experiments ($n = 3$); error bars represent SD.

to assess the reliability of the proposed fluorometric method. The results, summarized in Table 2, demonstrate consistent readings across all concentration levels. The low relative standard deviation (RSD, %) values confirm the high precision and reproducibility of the developed fluorometric assay.

3.6. Reproducibility and anti-interference/selectivity of DTT@C-AuNPs/OPA

The reproducibility of the proposed DTT@C-AuNPs/OPA system was evaluated by analyzing the fluorescence responses of eight independently prepared batches under identical conditions. The RSD values for the fluorescence intensities were calculated, with all values not exceeding 2.78%. These results indicate a high degree of reproducibility, confirming the reliability of the system for the quantification of AMD.

Furthermore, anti-interference and selectivity studies were performed to evaluate the applicability of the DTT@C-AuNPs/OPA system for real sample analysis. In this assessment, various potential interfering compounds—each at a concentration 20 times higher than that of AMD (20.0 μM)—were co-incubated with AMD under identical experimental conditions (Fig. 9). The results demonstrated that only AMD induced a significant enhancement in the fluorescence emission of the DTT@C-AuNPs/OPA system, while the presence of other compounds had negligible impact. The tested interfering substances included acyclovir, ribavirin, olaquindox, enrofloxacin, moxifloxacin, ciprofloxacin, ofloxacin, sulfamethazine, tetracycline, oxytetracycline, florfenicol, chloramphenicol, and metronidazole—compounds that may coexist with AMD in food samples. These findings confirm the high selectivity of the proposed system toward AMD. The high selectivity of the proposed DTT@C-AuNPs/OPA system toward AMD can be attributed to the well-established chemoselectivity of the OPA/thiol derivatization reaction, which proceeds efficiently only with primary aliphatic amines to yield highly fluorescent isoindole derivatives under mildly alkaline conditions.[43–45] Most

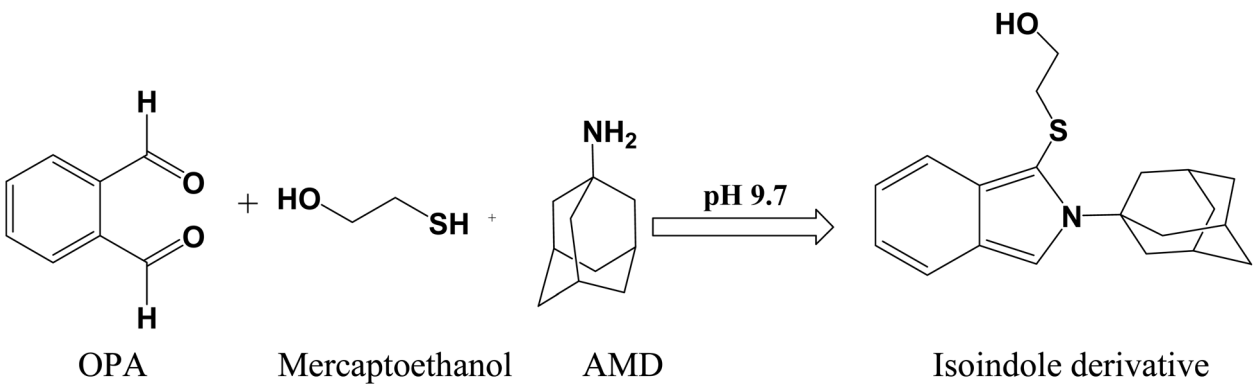

Scheme 2 Reaction between OPA, mercaptoethanol, and AMD (primary amine).

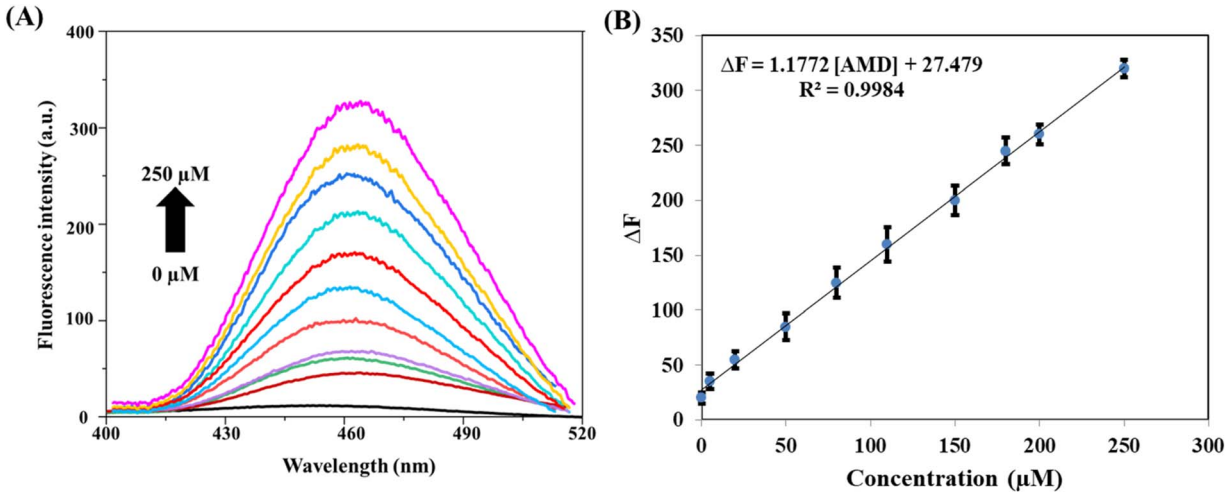

Fig. 7 (A) Fluorescence spectra of DTT@C-AuNPs/OPA after addition of AMD (0–250 µM) while (B) is calibration plot. Data are shown as mean ± SD from five independent experiments ($n = 5$); error bars represent SD.

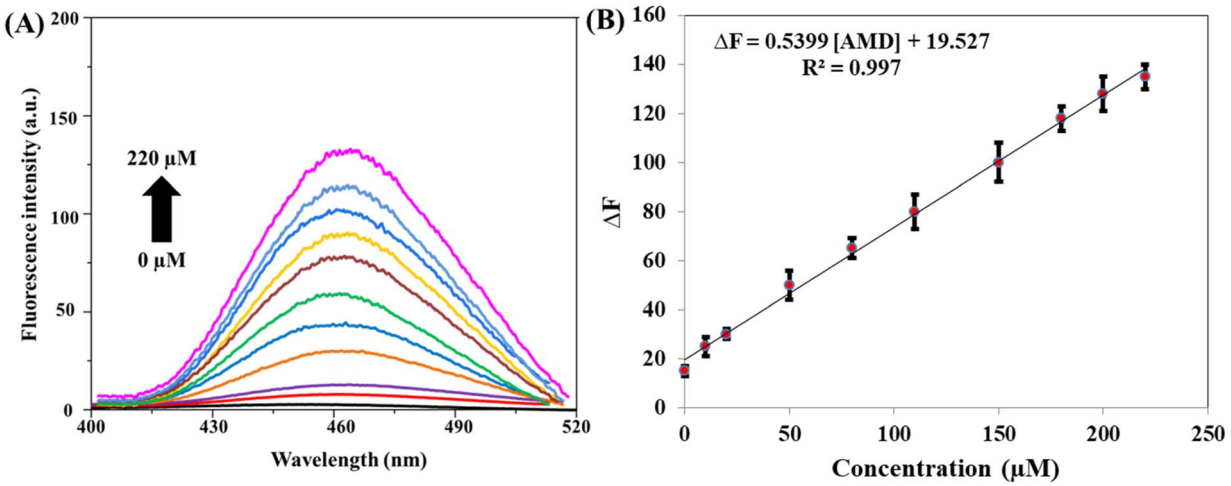

Fig. 8 (A) Fluorescence spectra of OPA/mercaptoethanol after addition of AMD (0–220 µM) while (B) is calibration plot. Data are shown as mean ± SD from five independent experiments ($n = 5$); error bars represent SD.

potential interferents tested in this study lack such reactive amine functionalities, resulting in negligible fluorescence response even at 20-fold higher concentrations. The covalent anchoring of DTT to AuNPs *via* Au–S bonding leaves one thiol group free to participate in isoindole formation, while surface confinement brings OPA, thiol, and AMD into close proximity, accelerating reaction kinetics and enhancing fluorescence quantum yield. This nanoscale microenvironment, combined with the negligible inner-filter effect at the working dilution, ensures that the observed "turn-on" signal originates from newly formed isoindole emission rather than from spectral artifacts. Together, these features provide both chemical and

Table 1 Comparison between proposed and other reported methods for AMD detection

Method	Probe	Linear range (µM)	LOD (µM)	Ref.
Colorimetry	Fe^{2+}-phen	2.6–65.7	0.78	36
	Fe^{2+}-bipy	3.9–144.7	3.8	
	Fe^{2+}/GOx/AuNPs	1.97×10^{-4} to 15.9	0.51×10^{-3}	37
	Colorimetric-based ELISA	—	0.033	38
Fluorometry	Cucurbit[8]uril/thionine	0.5–2.42	0.13	39
	DASP-β-CD	0–1000	1.0	40
	DTT@C-AuNPs	0.1–250	0.02	This work

Table 2 Precision of the proposed method ($n = 6$)

	Interday precision			Intraday precision		
Concentration (μM)	Found (μM)	Recovery (%)	RSD (%)	Found (μM)	Recovery (%)	RSD (%)
1.0	1.03	103.0	3.43	1.01	101.0	2.56
50.0	50.7	101.4	2.87	49.3	98.6	3.49
200.0	197.4	98.7	3.09	198.2	99.1	2.24

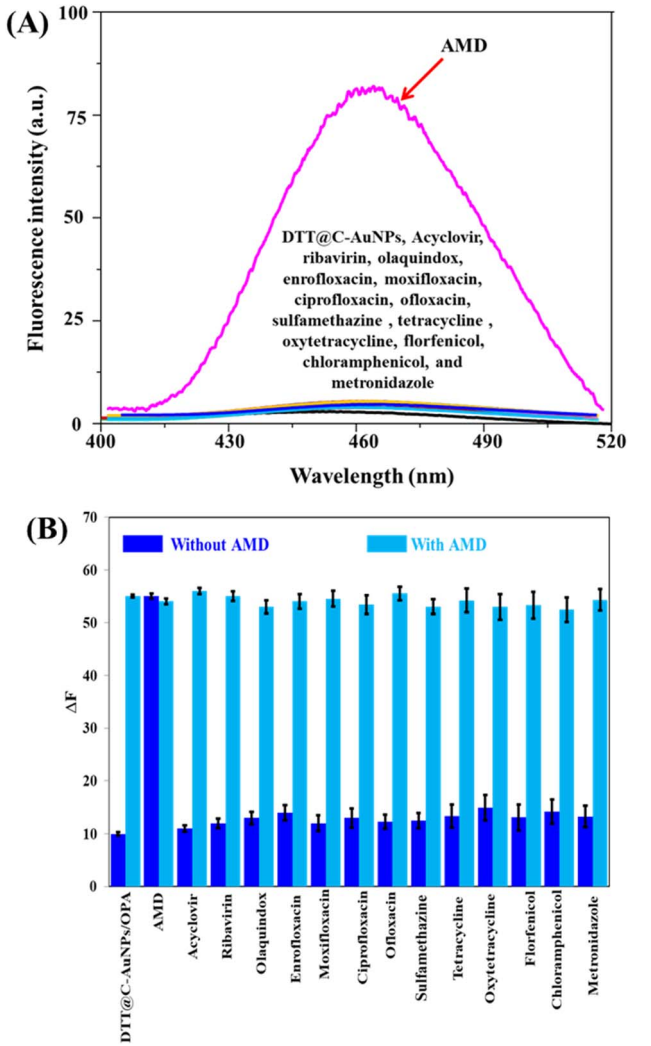

Fig. 9 (A) Fluorescence spectra of DTT@C-AuNPs/OPA system in presence of 20.0 μM AMD and 400 μM interfering species while (B) is bar diagram. Data are shown as mean ± SD from four independent experiments ($n = 4$); error bars represent SD.

physical bases for the superior selectivity of the assay toward AMD.

3.7. Applications

To evaluate the accuracy and robustness of the proposed fluorometric method for the detection of trace levels of AMD in complex food matrices, recovery studies were conducted using spiked egg, chicken, and duck tissue samples. Known concentrations of AMD standards (1.0, 5.0, and 10.0 μM) were added to each sample type to assess method performance across a range of expected contamination levels. As summarized in Table 3, the method demonstrated excellent recovery rates of 98.5–102.0% for egg samples, 97.9–103.2% for chicken, and 95.9–105.0% for duck, with relative standard deviations (RSDs) consistently below 3.88%. These results confirm the high precision and reproducibility of the assay and highlight its minimal susceptibility to matrix effects. Overall, the data validate the method's suitability for reliable quantitative analysis of AMD residues in diverse food products, supporting its potential application in food safety monitoring and regulatory compliance testing.

Table 3 Detection of AMD in food samples using DTT@C-AuNPs ($n = 6$)

Sample	Added (μM)	Found (μM)	Recovery (%)	RSD (%)
Egg	0.0	N.D.	—	—
	1.0	0.102	102.0	2.78
	5.0	4.963	99.3	3.25
	10.0	9.851	98.5	3.87
Chicken	0.0	N.D.	—	—
	1.0	1.032	103.2	1.78
	5.0	4.893	97.9	2.63
	10.0	9.942	99.4	3.49
Duck	0.0	N.D.	—	—
	1.0	0.105	105.0	2.65
	5.0	4.799	95.9	3.28
	10.0	10.043	100.4	3.88

4. Conclusion

A sensitive and selective fluorometric assay for the detection of amantadine (AMD) was developed based on isoindole formation *via* a ternary reaction involving OPA, DTT@C-AuNPs, and the primary amine group of AMD. The thiol-containing DTT enabled stable surface functionalization of the AuNPs while retaining a free –SH group to participate in the isoindole-forming reaction. Unlike conventional AuNP-based sensors that typically exhibit fluorescence quenching, this system operates as a fluorescence turn-on sensor, thereby enhancing detection sensitivity. Fluorescence measurements at 330 nm excitation showed a strong linear correlation between intensity and AMD concentration over a wide range (0.01–250 μM). Thanks to its fast reaction and the catalytic action of AuNPs, the

assay enables quick and reliable detection. Its accuracy and consistency were confirmed through comparison with the standard OPA method. When applied to real food matrices such as egg, chicken, and duck samples, the assay demonstrated high precision, low matrix interference, and excellent recovery rates. These findings underscore the assay's potential for practical application in routine food safety monitoring and regulatory compliance for AMD residue detection.

Conflicts of interest

The authors declare no competing interests.

Data availability

Data will be available upon request from the corresponding authors.

Acknowledgements

This work was supported and funded by the Deanship of Scientific Research at Imam Mohammad Ibn Saud Islamic University (IMSIU) (grant number IMSIU-DDRSP2501).

References

1 R. Tominack and F. Hayden, Rimantadine hydrochloride and amantadine hydrochloride use in influenza A virus infections, *Infect. Dis. Clin. North. Am.*, 1987, **1**, 459–478.
2 M. Foller, C. Geiger, H. Mahmud, J. Nicolay and F. Lang, Stimulation of suicidal erythrocyte death by amantadine, *Eur. J. Pharmacol.*, 2008, **581**, 13–18.
3 L. Nováková, J. Pavlík, L. Chrenková, O. Martinec and L. Červený, Current antiviral drugs and their analysis in biological materials—Part I: antivirals against respiratory and herpes viruses, *J. Pharm. Biomed. Anal.*, 2018, **147**, 400–416.
4 M. von Itzstein, The war against influenza: discovery and development of sialidase inhibitors, *Nat. Rev. Drug Discovery*, 2007, **6**, 967–974.
5 Z. Wang, K. Wen, X. Zhang, X. Li, Z. Wang, J. Shen and S. Ding, New Hapten synthesis, antibody production, and indirect competitive enzyme-linked immunosorbent assay for amantadine in chicken muscle, *Food Anal. Methods*, 2018, **11**(1), 302–308.
6 S. B. Turnipseed, J. M. Storey, W. C. Andersen, M. S. Filigenzi, A. S. Heise, J. J. Lohne, M. R. Madson, O. Ceric and R. Reimschuessel, Determination and confirmation of the antiviral drug amantadine and its analogues in chicken jerky pet treats, *J. Agric. Food Chem.*, 2015, **63**(31), 6968–6978.
7 J. Yang, M. Pan, K. Liu, X. Xie, S. Wang, L. Hong and S. Wang, Core-shell AuNRs@Ag-enhanced and magnetic separation-assisted SERS immunosensing platform for amantadine detection in animal-derived foods, *Sens. Actuators, B*, 2021, **349**, 130783.
8 X. Ma, S. He, Y. Zhang, J. Xu, H. Zhang, Z. Wang, J. Xue, X. Li, W. Yu and X. Fan, Signal-off tuned signal-on (SF-T-SN) colorimetric immunoassay for amantadine using activity-metal modulated peroxidase-mimicking nanozyme, *Sens. Actuators, B*, 2020, **311**, 127933.
9 S. Wu, F. Zhu, L. Hu, J. Xia, G. Xu, D. Liu, Q. Guo, K. Luo and W. Lai, Development of a competitive immunochromatographic assay for the sensitive detection of amantadine in chicken muscle, *Food Chem.*, 2017, **232**, 770–776.
10 M. Pan, J. Yang, S. Li, G. Wang, J. Wang and S. Wang, Indirect competitive ELISA and colloidal gold-based immunochromatographic strip for amantadine detection in animal-derived foods, *Anal. Methods*, 2019, **11**, 2027–2032.
11 X. Hao, N. Li, Z. Xu, N. B. Li and H. Q. Luo, An electrochemical sensing strategy for amantadine detection based on competitive host-guest interaction of methylene blue/beta-cyclodextrin/Poly(N-acetylaniline) modified electrode, *Electroanalysis*, 2016, **28**(7), 1489–1494.
12 H. Wang, S. M. Wang, W. Zhao, H. Y. Chen and J. J. Xu, Single particle plasmonic and electrochemical dual mode detection of amantadine, *Anal. Chim. Acta*, 2022, **1209**, 339838.
13 A. M. Mahmoud, S. S. Abu-Alrub, A. O. Al-Qarni, M. M. El-Wekil and R. Y. Shahin, A reliable and selective ratiometric sensing probe for fluorometric determination of $P_2O_7^{4-}$ based on AIE of GSH@CuNCs-assisted by Al-N@CQDs, *Spectrochim. Acta, Part A*, 2024, **310**, 123850.
14 J. Shen and Z. Fan, Construction of nanohybrid Tb@CDs/GSH-CuNCs as a ratiometric probe to detect phosphate anion based on aggregation-induced emission and FRET mechanism, *Microchim. Acta*, 2023, **190**, 427.
15 K. Alhazzani, A. Z. Alanazi, A. M. Alaseem, S. A. Al Awadh, S. A. Alanazi, A. A. AlSayyari, M. M. Alanazi and M. M. El-Wekil, A reliable ratiometric fluorescence sensing of heparin and its antidote based on cationic carbon quantum dots and acid red 87, *Microchem. J.*, 2023, **190**, 108666.
16 F. C. Church, H. E. Swaisgood, D. H. Porter and G. L. Catignani, Spectrophotometric assay using o-phthalaldehyde for determination of proteolysis in milk and isolated milk proteins, *J. Dairy Sci.*, 1983, **66**, 1219–1227.
17 S. S. J. R. Simons and D. F. Johnson, The structure of the fluorescent adduct formed in the reaction of o-phthalaldehyde and thiols with amines, *J. Am. Chem. Soc.*, 1976, **98**, 7098–7099.
18 X. Qi, W.-F. Wang, J. Wang, J.-L. Yang and Y.-P. Shi, Highly selective colorimetric detection of putrescine in fish products using o-phthalaldehyde derivatization reaction, *Food Chem.*, 2018, **259**, 245–250.
19 L. Chen, J. Li, S. Wang, W. Lu, A. Wu, J. Choo and L. Chen, FITC functionalized magnetic core–shell Fe_3O_4/Ag hybrid nanoparticle for selective determination of molecular biothiols, *Sens. Actuators, B*, 2014, **193**, 857–863.
20 K. Thomas and P. Kamat, Chromophore-functionalized gold surface binding properties of capped Au, *Acc. Chem. Res.*, 2003, **36**, 888–898.
21 B. Bekdeşer, S. E. Çelik, M. Bener, F. Dondurmacıoğlu, E. Yıldırım, E. N. Yavuz and R. Apak, Determination of

primary and secondary oxidation products in vegetable oils with gold nanoparticle based fluorometric turn-on nanosensor: A new total oxidation value, *Food Chem.*, 2024, **434**, 137426.

22 G. Frens, Controlled nucleation for the regulation of the particle size in monodisperse gold suspensions, *Nat. Phys. Sci.*, 1973, **241**, 20–22.

23 W. L. Tseng, K. H. Lee and H. T. Chang, Using nile red-adsorbed gold nanoparticles to locate glutathione within erythrocytes, *Langmuir*, 2005, **21**, 10676–10683.

24 Y. S. Alqahtani, A. M. Mahmoud, M. M. Khateeb, R. Ali and M. M. El-Wekil, Near-infrared fluorescent probe for selective and sensitive detection of glutathione based on thioctic acid-functionalized Ag/Au NCs-assisted by ferric ion, *Microchem. J.*, 2024, **201**, 110752.

25 H. Hakkinen, The gold-sulfur interface at the nanoscale, *Nat. Chem.*, 2012, **4**, 443–455.

26 W. W. Cleland, Dithiothreitol, A new protective reagent for SH groups, *Biochemistry*, 1964, **3**, 480–482.

27 Y. Wang and T. Bürgi, Ligand exchange reactions on thiolate-protected gold nanoclusters, *Nanoscale Adv.*, 2021, **3**, 2710–2727.

28 Z. Zhong, S. Patskovskyy, P. Bouvrette, J. H. T. Luong and A. Gedanken, The surface chemistry of Au colloids and their interactions with functional amino acids, *J. Phys. Chem. B*, 2004, **108**, 4046–4052.

29 J.-W. Park and J. S. Shumaker-Parry, Strong resistance of citrate anions on metal nanoparticles to desorption under thiol functionalization, *ACS Nano*, 2015, **9**(2), 1665–1682.

30 A. Cayuela, M. L. Soriano and M. Valcárcel, Reusable sensor based on functionalized carbon dots for the detection of silver nanoparticles in cosmetics via inner filter effect, *Anal. Chim. Acta*, 2015, **872**, 70–76.

31 S. K. Panigrahi and A. K. Mishra, Inner filter effect in fluorescence spectroscopy: as a problem and as a solution, *J. Photochem. Photobiol., C*, 2019, **41**, 100318.

32 H. Liu, M. Li, Y. Xia and X. Ren, A turn-on fluorescent sensor for selective and sensitive detection of alkaline phosphatase activity with gold nanoclusters based on inner filter effect, *ACS Appl. Mater. Interfaces*, 2017, **9**, 120–126.

33 L. Ceresa, J. Kimball, J. Chavez, E. Kitchner, Z. Nurekeyev, H. Doan, J. Borejdo, I. Gryczynski and Z. Gryczynski, On the origin and correction for inner filter effects in fluorescence. Part II: secondary inner filter effect – the proper use of front-face configuration for highly absorbing and scattering samples, *Methods Appl. Fluoresc.*, 2021, **9**, 035005.

34 N. M. El-Enany, D. T. El-Sherbiny, A. A. Abdelal and F. F. Belal, Validated Spectrofluorimetric Method for the Determination of Lamotrigine in Tablets and Human Plasma Through Derivatization with o-phthalaldehyde, *J. Fluoresc.*, 2010, **20**, 463–472.

35 H. M. A. Hassan, I. H. Alsohaimi, M. Y. El-Sayed, I. I. Ali, A. M. El-Didamony, H. A. Altaleb and M. S. Alshammari, Selective spectrofluorimetric approach for the assessment of two antipsychotic drugs through derivatization with O-phthalaldehyde, *Pharmaceuticals*, 2022, **15**, 1174.

36 H. A. Omara and A. S. Amin, Spectrophotometric microdetermination of anti-Parkinsonian and antiviral drug amantadine HCl in pure and in dosage forms, *Arabian J. Chem.*, 2011, **4**, 287–292.

37 W. Yu, T. Zhang, M. Ma, C. Chen, X. Liang, K. Wen, Z. Wang and J. Shen, Highly sensitive visual detection of amantadine residues in poultry at the ppb level: A colorimetric immunoassay based on a Fenton reaction and gold nanoparticles aggregation, *Anal. Chim. Acta*, 2018, **1027**, 130–136.

38 F. Zhu, J. Peng, Z. Huang, L. Hu, G. Zhang, D. Liu, K. Xing, K. Zhang and W. Lai, Specific colorimetric ELISA method based on DNA hybridization reaction and non-crosslinking gold nanoparticles aggregation for the detection of amantadine, *Food Chem.*, 2018, **257**, 382–387.

39 M. del Pozo, Á. Fernández and C. Quintana, On-line competitive host-guest interactions in a turn-on fluorometric method to amantadine determination in human serum and pharmaceutical formulations, *Talanta*, 2018, **179**, 124–130.

40 F. Fang, Z. Zhang, P. Zhang, X. Zhang, H. Ma and Y. Wei, Fluorescence detection of amantadine based on competitive β-Cyclodextrin host-guest inclusion process, *Colloids Surf., A*, 2024, **681**, 132801.

41 T. Zhang, J. Liua and J. P. Wang, Preparation of a molecularly imprinted polymer based chemiluminescence sensor for the determination of amantadine and rimantadine in meat, *Anal. Methods*, 2018, **10**, 5025–5031.

42 S. Sasse, A. Arrizabalaga-Larrañaga and S. S. Sterk, Antiviral drugs in animal-derived matrices: A review, *Heliyon*, 2024, **10**, e37460.

43 Y. Higashi, I. Uemori and Y. Fujii, Simultaneous determination of amantadine and rimantadine by HPLC in rat plasma with pre-column derivatization and fluorescence detection for pharmacokinetic studies, *Biomed. Chromatogr.*, 2005, **19**, 655–662.

44 P. D. Tzanavaras, S. Papadimitriou and C. K. Zacharis, Automated stopped-flow fluorimetric sensor for biologically active adamantane derivatives based on zone fluidics, *Molecules*, 2019, **24**, 3975.

45 M. Ntorkou, P. D. Tzanavaras and C. K. Zacharis, One step derivatization and switchable hydrophilicity solvent-based microextraction for the determination of adamantane analogues in human urine by HPLC-FLD, *Adv. Sample Prep.*, 2024, **12**, 100135.